Uncovering extreme nonlinear dynamics in solids through time-domain field analysis

P. D. Keathley,[1,*,†] S. V. B. Jensen,[2,*] M. Yeung,[1] M. R. Bionta,[1,‡] and L. B. Madsen[2,§]
[1]*Research Laboratory of Electronics, Massachusetts Institute of Technology, Cambridge, Massachusetts 02139, USA*
[2]*Department of Physics and Astronomy, Aarhus University, DK-8000 Aarhus C, Denmark*

(Received 21 October 2022; revised 23 January 2023; accepted 24 January 2023; published 3 February 2023)

We show that time-domain analysis of high harmonic generation from solids with subcycle resolution and broad, continuous spectral coverage is now experimentally viable due to the emergence of sensitive, solid-state optical-field-sampling techniques. With this experimental opportunity in mind, we use time-dependent density functional theory to explore what insights such a time-domain, field-resolved analysis might uncover about the extreme nonlinear electron dynamics responsible for high-harmonic generation (HHG) within solids. We illustrate how simple, visual analysis of the time-domain fields provides clear insight into the interplay between intra- and interband dynamical processes underlying nonlinear light generation when spectral signatures do not. Importantly, we observe conditions where the dominant emission mechanism suddenly switches from intra- to interband over a subcycle region of time within the pulse envelope of the driving wave form. This complex field response means that phase-resolved techniques requiring a certain level of periodicity are, in general, inadequate for the study of HHG from solids. We find that field-resolved measurements having both subcycle time resolution and broad, nearly continuous spectral coverage are required for a general understanding of solid-state HHG.

DOI: 10.1103/PhysRevB.107.054302

I. INTRODUCTION

High-harmonic generation (HHG) has proved a fruitful medium for studying extreme nonlinear interactions between intense pulses of light and matter. Through the study of HHG in atoms and molecules, we have developed a deep understanding of how energy is exchanged between light and electrons on the attosecond timescale [1]. As this work has grown and matured, it has ushered in the rapidly developing fields of attosecond science and technology [2].

In the past decade, researchers have begun exploring HHG from solid-state systems [3–6]. Compared to atomic and molecular systems, solid-state systems open new avenues for fundamental exploration. Due to the added role of the solid's band structure and the importance of electron-electron interactions, HHG in solids promises to be an interesting tool for probing attosecond to femtosecond dynamical interactions between light and a variety of materials. Indeed, HHG in solids has already been used to reconstruct band structure properties of solids [7–10], to measure the Berry curvature [11], and to track phase transitions in strongly correlated materials [12]. Unfortunately, along with these new avenues for exploration comes additional complexity in experimental analysis. In particular, both intraband and interband processes result in harmonics with similar nonperturbative intensity scaling laws. These similarities make it difficult, and in some cases impossible, to use spectral information alone to disentangle the physical mechanisms underlying HHG in solids.

Both theoretical and experimental works [7,13–16] show that field-sensitive information is critical to understanding HHG in solids as the harmonic fields carry unique signatures of the underlying emission mechanisms. While prior work has focused on field-sensitive information gained through phase- and polarization-resolved measurements [7,14–17], characterization of the harmonic field wave forms in the time domain would provide more detailed insights into the underlying dynamics of the generation process.

An *ex situ* field-sampling approach would be ideal for examining the origins of extreme nonlinearities in solids across a variety of material platforms. Beyond resolving fundamental scientific questions, the sampling of harmonic fields is also vital to the eventual use of HHG from solids in applications designed to leverage the attosecond-scale temporal structure of the harmonic field wave forms in time. Motivated by recent advances in experimental methods for petahertz-scale optical-field sampling [18–25], here we investigate (1) the viability of petahertz-scale field-sampling techniques with subcycle resolution for experimentally measuring harmonic fields directly in the time domain and (2) the physics revealed through a time-domain analysis of the high-harmonic fields generated in solids.

In Sec. II we perform numerical simulations showing that emerging optical-field-sampling techniques, in particular those that leverage field-driven tunneling ionization [26,27] and metallic nanostructures for field enhancement [25,28], place such measurements within reach. Using time-dependent density functional theory (TDDFT), we generate realistic HHG field wave forms [29,30]. We then show that the application of tunneling ionization with a perturbation for the

*These authors contributed equally to this work.
†pdkeat2@mit.edu
‡Present address: Linac Coherent Light Source, SLAC National Accelerator Laboratory, Menlo Park, California 94025, USA.
§bojer@phys.au.dk

time-domain observation of an electric field (TIPTOE) from metallic systems provides enough resolution to sample the high-harmonic fields with subcycle resolution into the UV range.

Having established the potential for nanoscale TIPTOE techniques to provide time-domain, field-resolved characterization of HHG in solids, in Sec. III we further study the kinds of time-domain field structures that such analysis would reveal. While they are often calculated, the time-domain field wave forms of solid-state HHG are often not reported or studied in detail. We examine how the interplay between the intra- and interband emission channels manifests in time-domain field signatures and discuss simple, visual methods for isolating the dominant emission physics using only the time-domain field information. We show that the time-domain structure of the generated harmonic fields naturally and simply reveals the dominant HHG emission mechanisms and their corresponding electron dynamics. Using Fourier analysis, we break apart and study the temporal structure of both intraband and interband processes in further detail. We observe that only moderate changes in peak intensity and central driving wavelength can alter the dominant emission mechanism, resulting in dramatic changes to the temporal structure of the harmonic fields despite minimal changes observed in the HHG spectra.

Importantly, our time-domain field analysis in Sec. III also shows that, unlike HHG from gases, with HHG from solids it cannot be assumed, even for driving pulses containing tens of cycles, that the emitted fields are semiperiodic in time. To our knowledge, this observation has yet to be discussed in the present literature and is of critical importance in guiding the experimental methods used for analysis of HHG in solids. In particular, we observe that under certain conditions the dominant emission mechanism can suddenly switch from intra- to interband dominant over a subcycle region of time within the pulse envelope of the driving wave form. This complex emission process and resulting lack of periodic structure in the generated harmonic fields mean that phase-resolved techniques requiring a certain level of periodicity are, in general, inadequate for the study of HHG from solids (e.g., techniques similar to reconstruction of attosecond beating by interference of two-photon transitions (RABBITT) that track the interference phase from harmonic to harmonic [14,31]). While these techniques certainly provide valuable insight, based on our findings, they must be interpreted and applied with caution. We find that, in general, measurements having both subcycle time resolution and broad, nearly continuous spectral coverage are required for a general understanding of solid-state HHG.

II. SAMPLING HHG FIELDS

In this section, we examine the experimental viability of performing time-domain field analysis of HHG from solids. There are two fundamental constraints that have to be satisfied. First, adequate temporal resolution of the field measurement process is required. The needed resolution to capture up to the Nth harmonic would be roughly $T_{\mathrm{cyc,D}}/(2N)$, where $T_{\mathrm{cyc,D}}$ is the cycle time of the driving field, given by $T_{\mathrm{cyc,D}} = \lambda_{\mathrm{D}}/c$, where λ_{D} is the driving wavelength and c is the speed of light. For example, assuming a driving wavelength of 2 μm, to capture the time-domain field information up to the ninth harmonic would require a temporal resolution of roughly 370 as or better. Second, the technique has to have adequate sensitivity to the signal field. Given the driving field strengths for the results in Sec. III are on the order of $0.5\,\mathrm{GVm}^{-1}$ and assuming a generation efficiency on the order of 10^{-6}, we can estimate that a sensitivity to harmonic field strengths on the order of MVm^{-1} is needed.

Several techniques for sampling optical fields with few- to subfemtosecond resolution have now been demonstrated [18–25,32]. Among these, TIPTOE has shown particular promise for the purpose of sampling HHG from solids [26,27]. The TIPTOE technique leverages the subfemtosecond electron tunneling response from gas-phase and solid-state systems driven by strong optical fields [22,25–28]. In the gas phase, TIPTOE has demonstrated the capability of sampling fields with frequencies in excess of 1 PHz [27] (i.e., subfemtosecond temporal resolution). More recently, it was shown that the sensitivity of TIPTOE can be significantly enhanced using arrays of nanostructures [25,28]. In particular, in Ref. [25] sensitivity down to $600\,\mathrm{kVm}^{-1}$ was demonstrated in the near infrared using gold nanoantennas. This sensitivity is already within the range desired for sampling HHG from solids and can be further improved through the use of larger array sizes or further averaging. While there are certainly alternative methods that offer the requisite bandwidth, as shown in Ref. [18], these alternative methods have thus far required orders of magnitude higher signal field strengths, placing them far out of reach for sampling HHG from solids. Encouraged by this potential combination of bandwidth and sensitivity, in the following we further explore the feasibility of a TIPTOE measurement based on optical tunneling from a metal for the field-resolved characterization of HHG from solids.

We show a notional schematic for the sampling of HHG from a solid-state system using TIPTOE in Fig. 1(a). An external laser pulse is incident on a beam splitter with the transmitted pulse becoming the driving field $E_{\mathrm{D}}(t)$ for the HHG and the reflected field becoming the gate field $E_{\mathrm{G}}(t)$ for driving the TIPTOE measurement. The generated field $E_{\mathrm{gen}}(t)$ is filtered by the dichroic mirror in order to isolate harmonic orders (HOs) such that measured HOs $\geqslant 2$. The reflected harmonic fields become the signal $E_{\mathrm{sig}}(t)$ for the TIPTOE measurement. In other words, $E_{\mathrm{sig}}(t)$ is the field resulting from filtering out the fundamental HO from the generated harmonics of $E_{\mathrm{gen}}(t)$. The delay of $E_{\mathrm{G}}(t)$ relative to $E_{\mathrm{sig}}(t)$ is referred to as τ, which is controlled by the lower delay stage. For the TIPTOE measurement, one records the oscillations of a cross-correlation current $I_{\mathrm{cc}}(\tau)$ generated via optical-field-driven tunneling from a gas-phase or solid-state system as a function of the delay τ. The cross-correlation current is approximated as

$$I_{\mathrm{cc}}(\tau) \propto \int_{-\infty}^{\infty} \left(\frac{d\Gamma}{dE}\bigg|_{E_{\mathrm{G}}(t-\tau)} \right) \times E_{\mathrm{sig}}(t)dt, \qquad (1)$$

where $\Gamma(E)$ is the tunneling rate as a function of field E [25,26]. Here we model the optical-field-driven tunneling from a metal surface using a Fowler-Nordheim emission rate as described in Refs. [25,33,34]. We note, however, that other

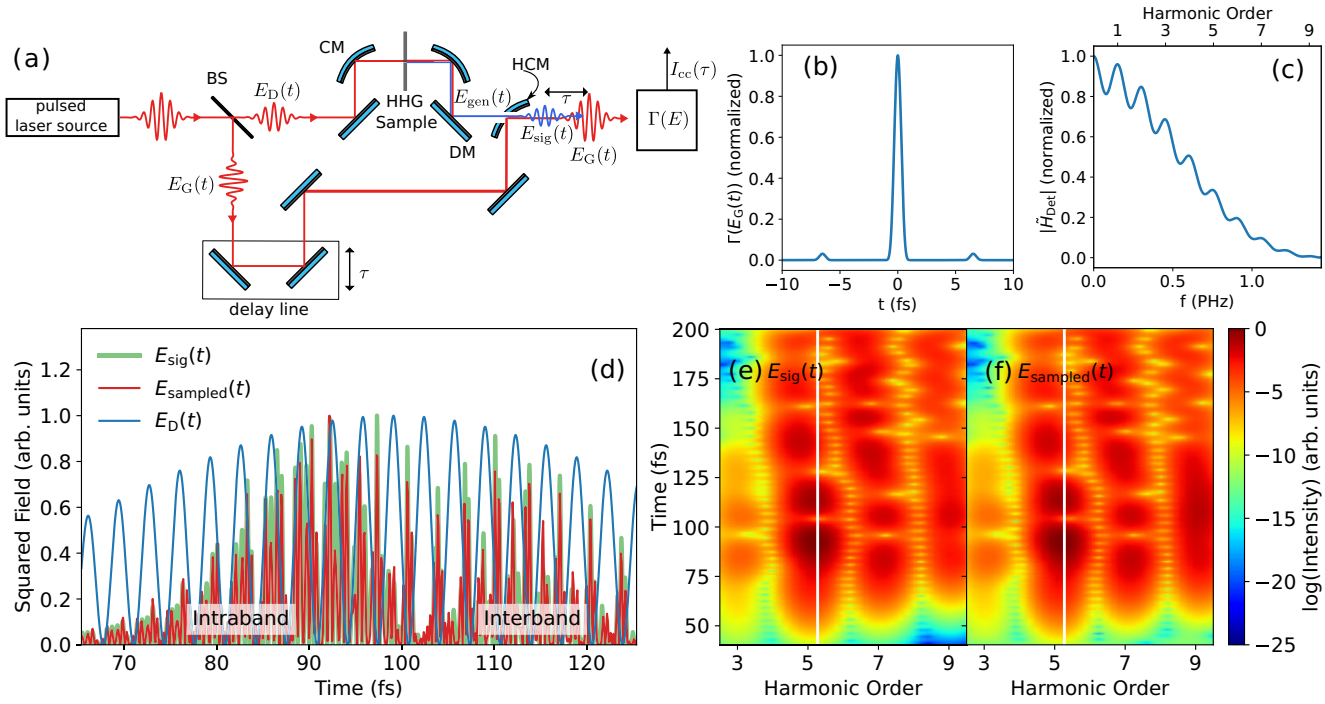

FIG. 1. Simulating harmonic field sampling using solid-state TIPTOE. (a) Notional schematic of the field-sampling experiment using TIPTOE. Abbreviations: BS, beam-splitter; CM, curved mirror; DM, dichroic mirror; HCM, holey curved mirror. (b) Calculation of $\Gamma(E_G(t))$ representing the instantaneous electron tunneling response from the metal surface. (c) Magnitude of the sampling transfer function $|\tilde{H}_{Det}(\omega)|$. (d)–(f) Comparison of direct TDDFT field output and the result of our simulation of the sampling response. (d) TDDFT output $|E_{sig}(t)|^2$ (shaded green line) and sampled field response $|E_{sampled}(t)|^2$ (solid red line) as a function of time. The insets denote temporal regions dominated by intra- or interband generation, which is described in detail in Sec. III. Gabor transform spectrograms of (e) the TDDFT fields and (f) sampled fields showing results up to the ninth harmonic. Here the white vertical line is inserted to illustrate the band gap energy of the HHG emitter.

systems, such as gases, semiconductors, and molecules, could be used for generating I_{cc}. Our choice was motivated by the ability of metals to achieve significant field enhancements for improved sensitivity to the signal field [25,28].

We start with a gate field $E_G(t)$ at the metal surface with a work function of 5.1 eV. The work function chosen is close to that of gold and is representative of most metals, with typical work functions varying between 4 and 6 eV. The gate field $E_G(t)$ was modeled as a Gaussian pulse having a central wavelength of 2 μm, full width at half maximum duration of 15 fs, and peak field strength of 7.5 GVm^{-1}. The tunneling response from the gate field $\Gamma(E_G(t))$ is plotted in Fig. 1(b). The peak gate field strength was chosen to be in line with prior work examining optical tunneling from solids [25,33,35,36] and to provide adequate temporal resolution. The pulse duration was chosen to ensure a single dominant subcycle emission window in time. We realize that the duration of the gate field in this case is shorter than that of the harmonic driving field. In practice, this could be accommodated via spectral filtering of a short pulse either as part of the transmission response of the beam splitter or as a separate element just after the beam splitter.

For the generation of realistic signal fields, we simulate HHG in band gap materials based on TDDFT [37]. This approach allows for a self-consistent *ab initio* investigation into the dynamics of a laser-driven many-body system. It succeeds in accounting for dynamical electron-electron interactions [38,39] and is suitable for describing experimental features [40]. Furthermore, TDDFT has been vital to study the mechanisms of HHG in solids [29], especially as the real-space description allows for introducing dopants [41], topology [42], or finite-system behavior [43,44]. For technical details on the TDDFT simulations see Appendix A.

We use a generic model of a band gap material with a band gap energy of roughly 3.3 eV. We apply a driving field with a central wavelength of 2 μm (≈0.62 eV) and a pulsed vector potential $A_D(t)$ with a 30-cycle $\sin^2$ envelope function. Here the subscript D denotes the driving pulse, with $E_D(t) = -\partial_t A_D(t)$. For the simulations shown in Figs. 1(d)–1(f) we used a peak driving intensity of 5×10^{10} W cm^{-2}. We illustrate this condition here as it generated the most complex dynamics of all conditions we investigated for this work.

We take the signal field $E_{sig}(t)$ to be that of the harmonic fields generated by our TDDFT simulations. The peak HHG field strength was taken to be 1 MVm^{-1}. We then calculated the cross-correlation current $I_{cc}(\tau)$ as defined in Eq. (1). The sampling process imposes its own transfer function $\tilde{H}_{Det}(\omega) = \mathcal{F}(\frac{d\Gamma}{dE}|_{E_D(t)})^*$, which is plotted in Fig. 1(c). To extract the sampled signal field information from $I_{cc}(\tau)$ we then calculated it by taking $E_{sampled}(t) = \mathcal{F}^{-1}\{\mathcal{F}(I_{cc})/\tilde{H}_{Det}(\omega)\}$. We note that in practice the electromagnetic response of the emitter structure (for example, that of a nanoantenna or nanostructured surface if it is being used for increased sensitivity) would also have to be accounted for in the calculation and analysis of $I_{cc}(\tau)$.

However, such a broad examination of various systems and their electromagnetic responses is beyond the scope of this work. Here we focus our attention on fundamental limitations arising from the tunneling response itself.

In Figs. 1(d)–1(f) we compare the harmonic signal fields to the sampled fields calculated through our solid-state TIPTOE analysis. Note that the sampled fields reconstruct the input fields with a high degree of accuracy. In particular, the sampled field output accurately tracks a sudden transition from intra- to interbandlike emission near 96 fs. In Sec. III we will explore in more detail how these contributions are determined through analysis of the temporal structure of the harmonic fields. But for now, we simply note the capability of accurately sampling subcycle signatures of the emitted field, which can reveal transitions in the dominant generation mechanism.

In Figs. 1(e) and 1(f) we compare the quality of the sampled data in greater detail using Gabor transformations of the TDDFT signal field and the TIPTOE sampled field. We calculate that the tunneling response has sufficient temporal resolution to accurately track the harmonic fields with no loss of information up to the ninth harmonic. Beyond the ninth harmonic, $|\tilde{H}_{\mathrm{Det}}(\omega)|$ drops off suddenly, as shown in Fig. 1(c), preventing accurate sampling of higher-frequency fields under the conditions simulated. However, the bandwidth might be extended by various means, for example, by using a metal with a higher work function, such as platinum (≈6.35 eV), to increase the nonlinearity of the tunneling response or by using a few-cycle gate pulse with a higher central frequency.

Having established TIPTOE from metallic systems as an attractive, emerging method for sampling harmonic fields in a single, *ex situ* measurement, in the next sections we explore the time-domain harmonic fields that would be revealed by such measurements in further detail.

III. TIME-DOMAIN STUDIES OF HHG

In this section, we present an extended study of HHG wave forms in the time domain using TDDFT. In particular, we present an extended analysis of the impact of the driving field wavelength and intensity on the HHG wave forms. The motivation for the choice of TDDFT and an introduction to our calculations were provided in Sec. II, and an extended description is provided in Appendix A. We note that the use of the *ab initio* TDDFT approach allows us to conclude that the findings are unrelated to the application of a few-band model description.

For our study, we selected two driving wavelengths for comparison: 2 μm (≈0.62 eV) and 2.3 μm (≈0.54 eV). For each driving wavelength, a range of intensities was simulated. We focus on intermediate intensity levels on the order of 10^{10} W cm^{-2}. We expect equivalent dynamics for a wide range of systems if the laser parameters are modified to accommodate the specific material properties.

We start our analysis by examining the harmonic spectra shown in Fig. 2. While there are differences in the spectra, it is impossible from these spectral data alone to determine the interplay of underlying emission mechanisms. Both intra- and interband processes result in odd-order harmonic generation with nonperturbative scaling of the harmonic strength with intensity. As we will show, similar-looking spectra resulting from both mechanisms mask dramatic differences in the temporal field structure.

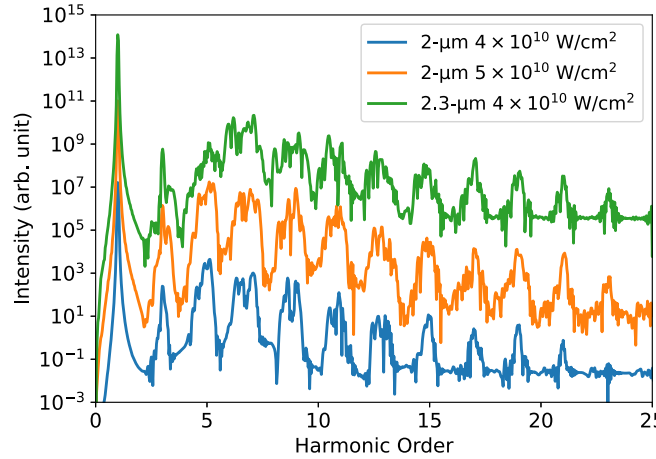

FIG. 2. Normalized high-harmonic spectra for each condition simulated: driving wavelength of 2 μm with a peak intensity of 4×10^{10} W cm^{-2} (bottom, blue curve), driving wavelength of 2 μm with a peak intensity of 5×10^{10} W cm^{-2} (middle, orange curve), and driving wavelength of 2.3 μm with a peak intensity of 4×10^{10} W cm^{-2} (top, green curve). Each curve is normalized differently for visual clarity. For each case the same system was used as a generation medium, with a band gap of roughly 3.3 eV.

For our time-domain study, we begin by examining the nonlinear system response from the 2-μm driver with a peak intensity of 4×10^{10} W cm^{-2}, as shown in Fig. 3. The squared electric field for HOs $\geqslant 2$ is shown in green. This field was calculated by applying a high-pass filter to remove the fundamental response oscillating at the driving frequency. It is useful for analysis to plot the square of the driving field (blue curve) and vector potential (orange curve) as a guide to the eye. As has been noted in prior work, intra- and interband responses can be distinguished by their phase relationship with the driving field and vector potential [13,15]. Specifically, the interband response is concentrated under the peaks of the squared vector potential (zeros of the squared field), and the intraband response is concentrated under the peaks of the squared driving field (zeros of the vector potential) [13]. Note that for the total nonlinear response in Fig. 3(a), the concentration of harmonic emission aligns with the peaks of the squared electric field, consistent with a dominance of intraband processes in the overall high-harmonic emission response.

When the time-dependent field is at hand through measurement, it is possible to perform more detailed analysis. For example, through Fourier analysis, it is possible to peel apart the emission behavior even further by examining the time-domain squared field response of selected harmonic regions. Such an analysis is shown in Figs. 3(b) and 3(c). In Fig. 3(b) we look at the fields generated from only HOs 3–7, and in Fig. 3(c) we look at the fields from only HOs 7–11. Note that we chose to break apart the response at HO 7 as this is just above the band gap energy of the material (3.3 eV lies between HOs 5 and 6). The majority of the harmonics below the band gap have an intraband character with high-harmonic energy concentrated under the peaks of the squared driving

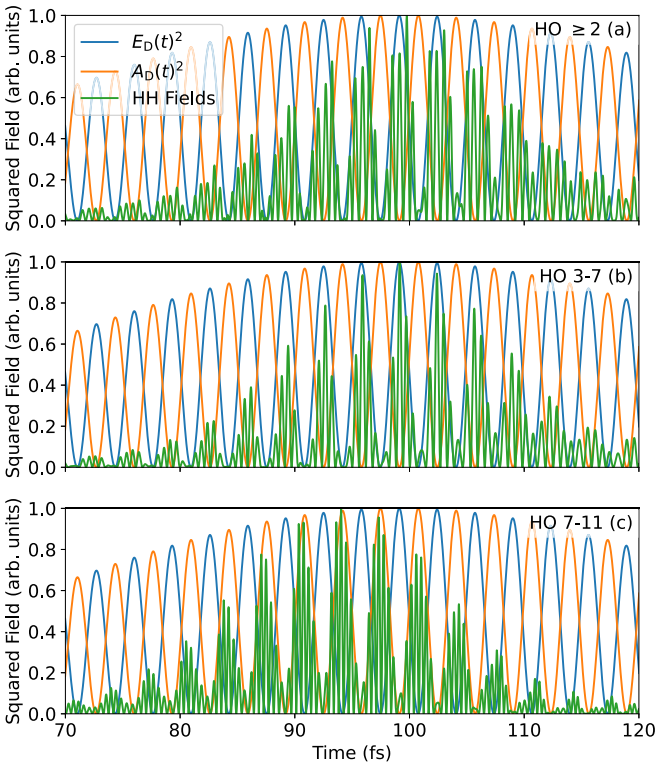

FIG. 3. Time-domain fields generated by various harmonic contributions for a driving wavelength of 2 μm and peak intensity of 4×10^{10} W cm^{-2}. (a) All HOs $\geqslant 2$, (b) HOs from 3 to 7, and (c) HOs from 7 to 11.

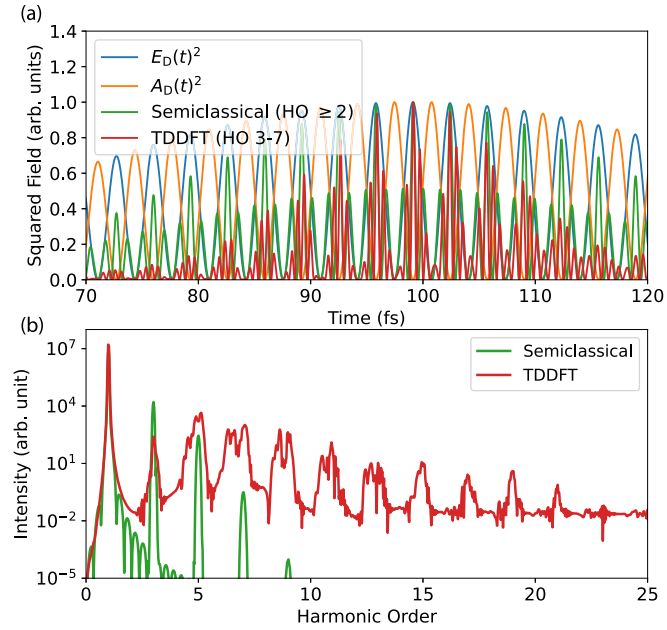

FIG. 4. Comparison between the semiclassical and TDDFT models. All driving conditions are the same as for Fig. 3. (a) Time-domain fields for all generated HOs $\geqslant 2$ for the semiclassical model (green) and HOs 3–7 for the TDDFT model. Note that just like for the lower HO of the TDDFT model, the semiclassical model predicts high-order harmonic fields that are concentrated under peaks of the square of the driving electric field. (b) A comparison of the spectra of the two models. The semiclassical model is dominated by the lower-order harmonics and drops off rapidly with increasing HO. On the other hand, due to the presence of interband processes and richer accounting of electron-electron interactions, an extended plateau forms in the TDDFT response. The TDDFT harmonics have rich structuring and a broader bandwidth in comparison with the harmonics predicted by the simple semiclassical response.

field. This is in stark contrast to harmonics above the band gap, which have an interband character, with high-harmonic energy concentrated under the peaks of the squared vector potential (zeros of the driving field).

To gain insight into the time-domain behavior of the intraband generation process it is useful to consider the semiclassical model for an intraband electron wave packet [45,46]. This model has been applied to understand various features of HHG in solids in the long-wavelength regime [3,11,47–49]. For space- and time-inversion-symmetric samples, an intraband wave packet centered at position x and wave vector k is governed by $\dot{k} = -E_D(t)$ and $\dot{x} = \partial\varepsilon(k)/\partial k$, within the electric dipole approximation, where we use atomic units. Here $\varepsilon(k)$ denotes the dispersion, which we extract from the TDDFT calculation. We consider a single trajectory that is initiated at the Γ point with $k(t=0) = 0$ and $x(t=0) = 0$. Details of the semiclassical modeling are given in Appendix B. The generated field $E_{\mathrm{gen},x}(t)$ of the semiclassical intraband electron can be expressed from the current and fulfills the following equation:

$$E_{\mathrm{gen},x}(t) \propto \frac{dj_x(t)}{dt} = \left(\frac{d^2\varepsilon(k)}{dk^2}\bigg|_{k(t)} \right) \times E_D(t), \qquad (2)$$

where the curvature of the dispersion generally can be expressed from the effective mass tensor $m_{\mathrm{eff}}^{-1}(k) = d^2\varepsilon(k)/dk^2$. An outcome of this is two characteristics of the intraband generation mechanism: (1) the appearance of higher-order harmonics is a result of the nonparabolic curvature of the dispersion, and (2) the emission of intraband harmonics in the time domain is proportional to the driving electric field. This is observed in Fig. 4, where the emitted field vanishes when the driving electric field vanishes and has maxima under the driving electric field maxima.

When comparing the semiclassical response to the intraband-dominated below band gap harmonics of the TDDFT calculation in Fig. 4, one observes that a single trajectory of the semiclassical intraband model is not sufficient to explain the full dynamics of the multielectron system. When considering the interference of multiple semiclassical trajectories, we expect the spectral features to improve. The phase relationship with the driving electric field is, however, independent of the initial conditions for the semiclassical trajectories and will thus persist in the interference of multiple trajectories. This characteristic is clearly present in the below band gap TDDFT dynamics, providing a guideline to decipher signatures of the intraband generation processes in convoluted emission signals.

To study the impact of a change in driving wavelength on the time-domain fields, we repeat the above analysis while keeping the peak intensity fixed at 4×10^{10} W cm^{-2} but with a change in the driving wavelength to 2.3 μm, as shown

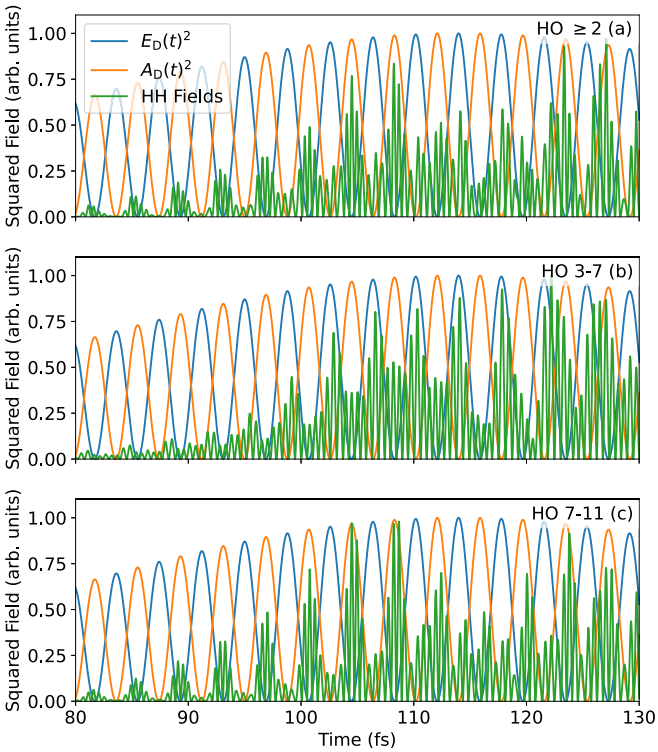

FIG. 5. Time-domain fields generated by various harmonic contributions for a driving wavelength of 2.3 μm and peak intensity of 4×10^{10} W cm^{-2}. (a) All HOs $\geqslant 2$, (b) HOs from 3 to 7, and (c) HOs from 7 to 11.

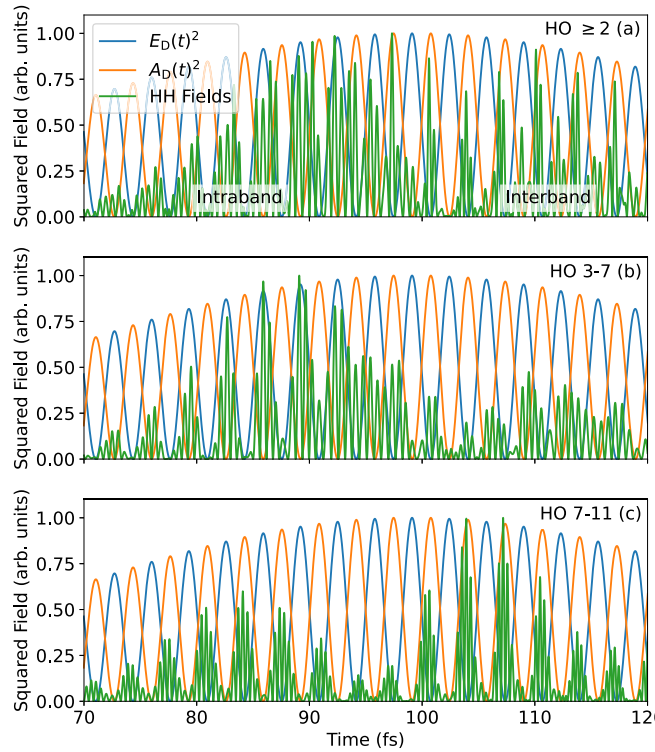

FIG. 6. Time-domain fields generated by various harmonic contributions for a driving wavelength of 2 μm and peak intensity of 5×10^{10} W cm^{-2}. (a) All HO $\geqslant 2$. Note the sudden transition from intraband- to interband-type radiation at $t \approx 95$ fs. (b) HO from 3 to 7 and (c) HO from 7 to 11.

in Fig. 5. Unlike for the 2-μm driver, now the emission is dominated by interbandlike emission, with the greatest field concentration under the peaks of the squared vector potential. The analysis of the HO regions generally follows the corresponding response from the 2-μm driver, with intrabandlike emission dominating emission from HO 3 to HO 7 and interbandlike emission dominating from HO 7 to HO 11. Referring back to Fig. 2, we note that the overall response is consistent with the shift in strength of the harmonics toward higher HOs for the case of the 2.3-μm driver relative to that of the 2-μm driver. Interestingly, the time-domain study also reveals that the harmonic radiation is less concentrated under the peaks of either the squared driving field or squared vector potential as for the case of the 2-μm driver.

Finally, we study the impact of a change to the peak driving intensity by keeping the driving wavelength fixed at 2 μm while increasing the peak intensity to 5×10^{10} W cm^{-2}, as shown in Fig. 6. Interestingly, for this case we observe a dramatic transition in the emission response from intraband dominant to interband dominant that occurs within the time window of the driving pulse envelope. In Fig. 6(a) we see that for times before roughly 96 fs the field energy is concentrated mainly under the peaks of the squared driving field, while just after 96 fs the fields rapidly concentrate under the peaks of the squared vector potential with a significant reduction in the duration of each half-cycle burst.

Looking at Figs. 6(b) and 6(c), we find on closer inspection that this switch in dominance occurs due to the unique character of the emission response within the time window of the pulse envelope from the two harmonic regions. At earlier times, HOs 3–7, exhibiting intrabandlike behavior, dominate the emission response. The half-cycle emission bursts in this window are concentrated under the peaks of the squared driving field and experience a sudden drop in intensity near 96 fs. On the other hand, the emission response for HOs 7–11 is dominant beyond 96 fs. As with earlier cases, these harmonics have an interband character with the field bursts concentrated under the peaks of the squared vector potential. They are also shorter in duration than for HOs 3–7. Further elucidating the origin of this change in the dominant generation process is not possible through analytical analysis due to the coupling between the generation processes [50]. An in-depth numerical analysis is therefore needed and will be considered for future work.

It is instructive to compare the Gabor transforms in Figs. 1(e) and 1(f) to the temporal response shown in Figs. 1(d) and 6(c). The drastic change observed in the time domain near 96 fs that is clearly shown in Fig. 1(d) is difficult to ascertain from a brief visual inspection of the Gabor transform and requires careful analysis. This is because at each region in time for the harmonic window resolvable by TIPTOE, the frequency content remains similar despite quite drastic changes in the relative temporal structure. In the Gabor transform, it is difficult to ascertain, without more detailed analysis, how the emission regime changes drastically from being intraband- to interbandlike in relation to the driving

fields and vector potential, while this transition is immediately apparent upon visual inspection of the time-domain fields.

Our findings in this section highlight the need for subcycle, field-resolved techniques in order to develop a full understanding of the precise temporal character of the high-harmonic radiation response in solids.

IV. SUMMARY AND CONCLUSION

In this work we explored the feasibility of emerging optical-field-sampling methods for the experimental time-domain analysis of high-harmonic fields generated in solids. Given the need for temporal resolution of hundreds of attoseconds and approximately megavolt per meter field sensitivity, we found the TIPTOE method [26,27] using a metallic tunneling medium [25,28] to be a compelling choice. Our calculations showed that under realistic experimental conditions, TIPTOE from metals offers sufficient temporal resolution and spectral coverage to enable time-domain harmonic field analysis throughout the infrared and visible spectral regions and just into the UV spectral region.

Through a study of realistic time-domain harmonic fields generated through TDDFT, we showed how a simple analysis of the time-domain field structure directly and visually reveals the relative contributions of intra- and interband emission mechanisms. In particular, we exploited the fact that the fields of intraband harmonics concentrate under the peaks of the squared driving field, while interband harmonics concentrate under the peaks of the squared vector potential, to study the interplay between these two emission mechanisms both as a function of HO and in time during the evolution of a single driving pulse.

For the system modeled in this work, we used this analysis to show that harmonics above the band gap were dominated by interband processes while those below the band gap were dominated by intraband processes but influenced by the coupling of both intra- and interband processes. Using Fourier analysis, we were able to isolate and study the temporal response of harmonics from both regimes. A semiclassical analysis of the intraband generation process provided an emission that was temporally confined to the shape of the driving electric field. This characteristic feature of intraband harmonics was compared to the many-electron TDDFT harmonic emission signal and was found to be useful as a guideline to decipher harmonics originating from intra- or interband mechanisms.

An important and consequential observation that arose from this study is that temporal field structures can arise where intra- and interband dominance evolves rapidly from one temporal region to another within the envelope of the driving pulse. Under the simulated conditions, we observed this evolution to occur over the duration of just a single cycle of the driving field. This leads to a highly aperiodic response, which stands in contrast to high harmonics from gas-phase systems which can remain relatively periodic for long driving pulses over a wide range of conditions. From this observation we conclude that time-averaged, phase-resolved techniques that assume the harmonics are well described as a quasiperiodic pulse train with a smooth envelope (e.g., RABBITT and related techniques) are inadequate for a general analysis of the dynamics of HHG in solids. While they provide useful and significant information, the results must be analyzed with care. For conditions where rapid shifts in emission dynamics like those observed in Fig. 6 are present, measurements having both subcycle time resolution and broad, nearly continuous spectral coverage are necessary.

Our findings strongly support the pursuit of time-domain field measurements for the analysis of HHG in solids. Methods for subcycle field analysis are rapidly advancing [18]. We are confident that these technologies will become instrumental for uncovering fundamental aspects of ultrafast strong-field processes in condensed matter directly in the time domain.

The simulation data and code used for analysis and plot generation for this work can be found on GitHub [51].

ACKNOWLEDGMENTS

This material is based in part upon work supported by the Air Force Office of Scientific Research under Award No. FA9550-18-1-0436. M.Y. acknowledges support from the National Science Foundation Graduate Research Fellowship Program, Grant No. 1745302. L.B.M. and S.V.B.J. acknowledge support from the Independent Research Fund Denmark (Grant No. 9040-00001B). S.V.B.J. further acknowledges support from the Danish Ministry of Higher Education and Science.

APPENDIX A: TDDFT SIMULATIONS

We represent the electrons by auxiliary noninteracting time-dependent Kohn-Sham (KS) orbitals $\varphi_{\sigma,i}(x,t)$ with spin $\sigma = \{\uparrow,\downarrow\}$, which are obtained by imaginary-time propagation. When driven by an electromagnetic field, described by the vector potential $A_{\mathrm{D}}(t)$, the electron dynamics can be captured along the laser polarization direction with a one-dimensional model. Thus, in atomic units, the electron-nuclear interaction is described with a static softened, $\epsilon = 2.25$, Coulomb potential $v_{\mathrm{ion}}(x) = -\sum_{i=0}^{N-1} Z[(x-x_i)^2 + \epsilon]^{-1/2}$ formed by a string of $N = 100$ ions of nuclear charge $Z = 4$ placed at $x_i = [i-(N-1)/2]a$ and separated by lattice constant $a = 5.3$. The KS orbitals are propagated through the time-dependent KS equation $i\partial_t \varphi_{\sigma,i}(x,t) = \{-\partial_x^2/2 - iA_{\mathrm{D}}(t)\partial_x + \tilde{v}_{\mathrm{KS}}[n_\sigma](x,t)\}\varphi_{\sigma,i}(x,t)$ using the Crank-Nicolson method with a predictor-corrector step and an absorbing boundary potential [52,53]. The time-dependent KS potential $\tilde{v}_{\mathrm{KS}}[\{n_\sigma\}](x,t) = v_{\mathrm{ion}}(x) + v_H[n](x,t) + v_{xc}[\{n_\sigma\}](x,t)$ contains the Hartree potential $v_H[n](x,t) = \int dx' n(x',t)[(x-x')^2+\epsilon]^{-1/2}$ and the local spin-density exchange-correlation potential $v_{xc}[\{n_\sigma\}](x,t) \simeq -[6n_\sigma(x,t)/\pi]^{1/3}$. These include the dynamic electron-electron interactions through the density $n(x,t) = \sum_{\sigma=\uparrow,\downarrow} n_\sigma(x,t)$ and spin density $n_\sigma(x,t) = \sum_{i=0}^{N_\sigma-1} |\varphi_{\sigma,i}(x,t)|^2$. We consider a charge- and spin-neutral system such that the number of electrons with a given spin is $N_{\uparrow,\downarrow} = ZN/2$. The spatial grid contains 21 250 grid points of size 0.1. Macroscopic propagation effects are not accounted for, as they are suppressed for thin targets [54,55], which can be produced for experiments [48]. Similarly, we disregard nondipole effects [49], as they are negligible when describing the generated field as $E_{\mathrm{gen},x}(t) \propto dj_x(t)/dt$, with $j_x(t)$ being

the current measured along the polarization axis of the driving field. A temporal grid with 95 000 grid points and a step of 0.1 ensured convergence.

APPENDIX B: SEMICLASSICAL SIMULATIONS

The intraband generation mechanism is clarified by a numerical simulation of the semiclassical equations. We use the symmetric dispersion in the vicinity of the Γ point of the previously obtained TDDFT band structure and expand as a Fourier series $\varepsilon(k) = [1 + \sum_n c_n \cos(nka)]/4a^2$, with coefficients $c_n = -37.4496\delta_{n,1} + 2.9303\delta_{n,2} - 3.6618\delta_{n,3} + 0.9685\delta_{n,4} - 1.1009\delta_{n,5} + 0.5821\delta_{n,6} - 0.4201\delta_{n,7} + 0.3697\delta_{n,8}$. We propagate a single-electron wave packet trajectory of the semiclassical equations, initiated at the Γ point, $k(t = 0) = 0$ at $x(t = 0) = 0$, as is commonly done in the literature [8,11,16]. Explicitly, for such material parameters, Eq. (2) can be further written as

$$E_{\mathrm{gen},x}(t) \propto -\left(\sum_n \frac{n^2 c_n}{4} \cos[naA_{\mathrm{D}}(t)]\right) \times E_{\mathrm{D}}(t). \quad \text{(B1)}$$

The first term, arising from the curvature of the dispersion, gives rise to the harmonic contributions in the generated electric field and is dependent on the initial conditions of the semiclassical wave packet. The second term is independent of initial conditions and confines the emitted field to the temporal shape of the driving electric field.

[1] P. B. Corkum and F. Krausz, Attosecond science, Nat. Phys. **3**, 381 (2007).

[2] F. Krausz and M. Ivanov, Attosecond physics, Rev. Mod. Phys. **81**, 163 (2009).

[3] S. Ghimire, A. D. DiChiara, E. Sistrunk, P. Agostini, L. F. DiMauro, and D. A. Reis, Observation of high-order harmonic generation in a bulk crystal, Nat. Phys. **7**, 138 (2011).

[4] S. Ghimire and D. A. Reis, High-harmonic generation from solids, Nat. Phys. **15**, 10 (2019).

[5] E. Goulielmakis and T. Brabec, High harmonic generation in condensed matter, Nat. Photonics **16**, 411 (2022).

[6] U. Huttner, M. Kira, and S. W. Koch, Ultrahigh off-resonant field effects in semiconductors, Laser Photonics Rev. **11**, 1700049 (2017).

[7] G. Vampa, T. J. Hammond, N. Thiré, B. E. Schmidt, F. Légaré, C. R. McDonald, T. Brabec, D. D. Klug, and P. B. Corkum, All-Optical Reconstruction of Crystal Band Structure, Phys. Rev. Lett. **115**, 193603 (2015).

[8] T. T. Luu, M. Garg, S. Y. Kruchinin, A. Moulet, M. T. Hassan, and E. Goulielmakis, Extreme ultraviolet high-harmonic spectroscopy of solids, Nature (London) **521**, 498 (2015).

[9] A. J. Uzan-Narovlansky, Á. Jiménez-Galán, G. Orenstein, R. E. F. Silva, T. Arusi-Parpar, S. Shames, B. D. Bruner, B. Yan, O. Smirnova, M. Ivanov, and N. Dudovich, Observation of light-driven band structure via multiband high-harmonic spectroscopy, Nat. Photonics **16**, 428 (2022).

[10] A. J. Uzan, G. Orenstein, Á. Jiménez-Galán, C. McDonald, R. E. F. Silva, B. D. Bruner, N. D. Klimkin, V. Blanchet, T. Arusi-Parpar, M. Krüger, A. N. Rubtsov, O. Smirnova, M. Ivanov, B. Yan, T. Brabec, and N. Dudovich, Attosecond spectral singularities in solid-state high-harmonic generation, Nat. Photonics **14**, 183 (2020).

[11] T. T. Luu and H. J. Wörner, Measurement of the berry curvature of solids using high-harmonic spectroscopy, Nat. Commun. **9**, 916 (2018).

[12] M. R. Bionta, E. Haddad, A. Leblanc, V. Gruson, P. Lassonde, H. Ibrahim, J. Chaillou, N. Émond, M. R. Otto, Á. Jiménez-Galán, R. E. F. Silva, M. Ivanov, B. J. Siwick, M. Chaker, and F. Légaré, Tracking ultrafast solid-state dynamics using high harmonic spectroscopy, Phys. Rev. Res. **3**, 023250 (2021).

[13] M. Wu, S. Ghimire, D. A. Reis, K. J. Schafer, and M. B. Gaarde, High-harmonic generation from Bloch electrons in solids, Phys. Rev. A **91**, 043839 (2015).

[14] G. Vampa, T. J. Hammond, N. Thiré, B. E. Schmidt, F. Légaré, C. R. McDonald, T. Brabec, and P. B. Corkum, Linking high harmonics from gases and solids, Nature (London) **522**, 462 (2015).

[15] M. Hohenleutner, F. Langer, O. Schubert, M. Knorr, U. Huttner, S. W. Koch, M. Kira, and R. Huber, Real-time observation of interfering crystal electrons in high-harmonic generation, Nature (London) **523**, 572 (2015).

[16] N. Klemke, O. D. Mücke, A. Rubio, F. X. Kärtner, and N. Tancogne-Dejean, Role of intraband dynamics in the generation of circularly polarized high harmonics from solids, Phys. Rev. B **102**, 104308 (2020).

[17] Y. Kobayashi, C. Heide, H. K. Kelardeh, A. Johnson, F. Liu, T. F. Heinz, D. A. Reis, and S. Ghimire, Polarization flipping of even-order harmonics in monolayer transition-metal dichalcogenides, Ultrafast Sci. **2021**, 9820716 (2021).

[18] A. Herbst, K. Scheffter, M. M. Bidhendi, M. Kieker, A. Srivastava, and H. Fattahi, Recent advances in petahertz electric field sampling, J. Phys. B **55**, 172001 (2022).

[19] S. Sederberg, D. Zimin, S. Keiber, F. Siegrist, M. S. Wismer, V. S. Yakovlev, I. Floss, C. Lemell, J. Burgdörfer, M. Schultze, F. Krausz, and N. Karpowicz, Attosecond optoelectronic field measurement in solids, Nat. Commun. **11**, 430 (2020).

[20] D. Zimin, M. Weidman, J. Schötz, M. F. Kling, V. S. Yakovlev, F. Krausz, and N. Karpowicz, Petahertz-scale nonlinear photoconductive sampling in air, Optica **8**, 586 (2021).

[21] M. Ossiander, K. Golyari, K. Scharl, L. Lehnert, F. Siegrist, J. P. Bürger, D. Zimin, J. A. Gessner, M. Weidman, I. Floss, V. Smejkal, S. Donsa, C. Lemell, F. Libisch, N. Karpowicz, J. Burgdörfer, F. Krausz, and M. Schultze, The speed limit of optoelectronics, Nat. Commun. **13**, 1620 (2022).

[22] Y. Liu, J. E. Beetar, J. Nesper, S. Gholam-Mirzaei, and M. Chini, Single-shot measurement of few-cycle optical waveforms on a chip, Nat. Photonics **16**, 109 (2022).

[23] B. Förg, J. Schötz, F. Süßmann, M. Förster, M. Krüger, B. Ahn, W. A. Okell, K. Wintersperger, S. Zherebtsov, A. Guggenmos, V. Pervak, A. Kessel, S. A. Trushin, A. M. Azzeer, M. I. Stockman, D. Kim, F. Krausz, P. Hommelhoff, and M. F. Kling, Attosecond nanoscale near-field sampling, Nat. Commun. **7**, 11717 (2016).

[24] E. Goulielmakis, M. Uiberacker, R. Kienberger, A. Baltuska, V. Yakovlev, A. Scrinzi, T. Westerwalbesloh, U. Kleineberg, U.

Heinzmann, M. Drescher, and F. Krausz, Direct measurement of light waves, Science **305**, 1267 (2004).

[25] M. R. Bionta, F. Ritzkowsky, M. Turchetti, Y. Yang, D. Cattozzo Mor, W. P. Putnam, F. X. Kärtner, K. K. Berggren, and P. D. Keathley, On-chip sampling of optical fields with attosecond resolution, Nat. Photonics **15**, 456 (2021).

[26] W. Cho, S. I. Hwang, C. H. Nam, M. R. Bionta, P. Lassonde, B. E. Schmidt, H. Ibrahim, F. Légaré, and K. T. Kim, Temporal characterization of femtosecond laser pulses using tunneling ionization in the UV, visible, and mid-IR ranges, Sci. Rep. **9**, 16067 (2019).

[27] S. B. Park, K. Kim, W. Cho, S. I. Hwang, I. Ivanov, C. H. Nam, and K. T. Kim, Direct sampling of a light wave in air, Optica **5**, 402 (2018).

[28] J. Blöchl, J. Schötz, A. Maliakkal, N. Šreibere, Z. Wang, P. Rosenberger, P. Hommelhoff, A. Staudte, P. B. Corkum, B. Bergues, and M. F. Kling, Spatiotemporal sampling of near-petahertz vortex fields, Optica **9**, 755 (2022).

[29] N. Tancogne-Dejean, O. D. Mücke, F. X. Kärtner, and A. Rubio, Impact of the Electronic Band Structure in High-Harmonic Generation Spectra of Solids, Phys. Rev. Lett. **118**, 087403 (2017).

[30] T. Otobe, High-harmonic generation in α-quartz by electron-hole recombination, Phys. Rev. B **94**, 235152 (2016).

[31] P. M. Paul, E. S. Toma, P. Breger, G. Mullot, F. Auge, P. Balcou, H. G. Muller, and P. Agostini, Observation of a train of attosecond pulses from high harmonic generation, Science **292**, 1689 (2001).

[32] S. Keiber, S. Sederberg, A. Schwarz, M. Trubetskov, V. Pervak, F. Krausz, and N. Karpowicz, Electro-optic sampling of near-infrared waveforms, Nat. Photonics **10**, 159 (2016).

[33] W. P. Putnam, R. G. Hobbs, P. D. Keathley, K. K. Berggren, and F. X. Kärtner, Optical-field-controlled photoemission from plasmonic nanoparticles, Nat. Phys. **13**, 335 (2017).

[34] P. D. Keathley, W. P. Putnam, P. Vasireddy, R. G. Hobbs, Y. Yang, K. K. Berggren, and F. X. Kärtner, Vanishing carrier-envelope-phase-sensitive response in optical-field photoemission from plasmonic nanoantennas, Nat. Phys. **15**, 1128 (2019).

[35] T. Rybka, M. Ludwig, M. F. Schmalz, V. Knittel, D. Brida, and A. Leitenstorfer, Sub-cycle optical phase control of nanotunnelling in the single-electron regime, Nat. Photonics **10**, 667 (2016).

[36] J. Schoetz, Z. Wang, E. Pisanty, M. Lewenstein, M. F. Kling, and M. F. Ciappina, Perspective on petahertz electronics and attosecond nanoscopy, ACS Photonics **6**, 3057 (2019).

[37] E. Runge and E. K. U. Gross, Density-Functional Theory for Time-Dependent Systems, Phys. Rev. Lett. **52**, 997 (1984).

[38] S. V. B. Jensen and L. B. Madsen, Edge-state and bulklike laser-induced correlation effects in high-harmonic generation from a linear chain, Phys. Rev. B **104**, 054309 (2021).

[39] N. Tancogne-Dejean and A. Rubio, Parameter-free hybridlike functional based on an extended Hubbard model: DFT $+ U + V$, Phys. Rev. B **102**, 155117 (2020).

[40] N. Tancogne-Dejean, O. D. Mücke, F. X. Kärtner, and A. Rubio, Ellipticity dependence of high-harmonic generation in solids originating from coupled intraband and interband dynamics, Nat. Commun. **8**, 745 (2017).

[41] C. Yu, K. K. Hansen, and L. B. Madsen, Enhanced high-order harmonic generation in donor-doped band-gap materials, Phys. Rev. A **99**, 013435 (2019).

[42] D. Bauer and K. K. Hansen, High-Harmonic Generation in Solids with and without Topological Edge States, Phys. Rev. Lett. **120**, 177401 (2018).

[43] K. K. Hansen, D. Bauer, and L. B. Madsen, Finite-system effects on high-order harmonic generation: From atoms to solids, Phys. Rev. A **97**, 043424 (2018).

[44] S. V. B. Jensen, H. Iravani, and L. B. Madsen, Edge-state-induced correlation effects in two-color pump-probe high-order harmonic generation, Phys. Rev. A **103**, 053121 (2021).

[45] N. W. Ashcroft, A. W, and N. D. Mermin, *Solid State Physics* (Holt, Rinehart and Winston, New York, 1976).

[46] G. Sundaram and Q. Niu, Wave-packet dynamics in slowly perturbed crystals: Gradient corrections and Berry-phase effects, Phys. Rev. B **59**, 14915 (1999).

[47] K. Kaneshima, Y. Shinohara, K. Takeuchi, N. Ishii, K. Imasaka, T. Kaji, S. Ashihara, K. L. Ishikawa, and J. Itatani, Polarization-Resolved Study of High Harmonics from Bulk Semiconductors, Phys. Rev. Lett. **120**, 243903 (2018).

[48] H. Liu, Y. Li, Y. S. You, S. Ghimire, T. F. Heinz, and D. A. Reis, High-harmonic generation from an atomically thin semiconductor, Nat. Phys. **13**, 262 (2017).

[49] S. V. B. Jensen and L. B. Madsen, Propagation time and nondipole contributions to intraband high-order harmonic generation, Phys. Rev. A **105**, L021101 (2022).

[50] D. Golde, T. Meier, and S. W. Koch, High harmonics generated in semiconductor nanostructures by the coupled dynamics of optical inter- and intraband excitations, Phys. Rev. B **77**, 075330 (2008).

[51] https://github.com/qnngroup/manu-uncovering-extreme-nonlinear-dynamics-in-solids-through-time-domain-field-analysis.git.

[52] *Computational Strong-Field Quantum Dynamics: Intense Light-Matter Interactions*, edited by D. Bauer, De Gruyter Graduate (De Gruyter, Berlin, 2017).

[53] R. Kosloff and D. Kosloff, Absorbing boundaries for wave propagation problems, J. Comput. Phys. **63**, 363 (1986).

[54] I. Kilen, M. Kolesik, J. Hader, J. V. Moloney, U. Huttner, M. K. Hagen, and S. W. Koch, Propagation Induced Dephasing in Semiconductor High-Harmonic Generation, Phys. Rev. Lett. **125**, 083901 (2020).

[55] S. Yamada and K. Yabana, Determining the optimum thickness for high harmonic generation from nanoscale thin films: An *ab initio* computational study, Phys. Rev. B **103**, 155426 (2021).